Oxidation and degradation of amorphous SiAlN coating via forming Si-Si bond

Zhaohe Gao[a*], Justyna Kulczyk-Malecka[b], Zhenbo Zhang[a] , Han Liu[a], Xinxin Zhang[a], Ying Chen[a], Patrick Hill[a], Peter Kelly[b] and Ping Xiao[a*]

[a]*Henry Royce Institute, Department of Materials, University of Manchester, Manchester, M13 9PL, UK*
[b]*Surface Engineering Group, Manchester Metropolitan University, Manchester, M1 5GD, UK*

Abstract: The oxidation and degradation of amorphous SiAlN coatings consisting of Si_3N_4 and AlN phases, with 750 nm or 300 nm Mo interlayers on Zr alloy in steam environment at 1000°C were investigated. After 1 hour exposure, no detectable oxide scale formed on SiAlN/Mo (750 nm) coatings whereas SiAlN/Mo (300 nm) formed oxide scale. The downward diffusion of Si followed by relatively fast downward diffusion of N generated excessive Si and lean N, forming Si-Si bond in outermost surface of SiAlN, thereby resulting in oxidation. The degradation mechanism of amorphous nitrides was determined by elemental composition instead of reported amorphous or crystalline status.

Keywords: FIB-XPS; Si-Si bond; SiAlN amorphous coating; Outward diffusion; Oxidation; Degradation,

*Corresponding authors:
zhaohe.gao@manchester.ac.uk (Z.G.); p.xiao@manchester.ac.uk (P.X.)

1. Introduction

Since Fukushima Daiichi Power Plant happened the nuclear power plant disaster in March 2011, the safety issues in case of a Loss-of-Coolant Accident (LOCA) in the Light Water Reactor have been raised [1-4]. One potential mitigating strategy is to deposit a protective coating onto the surface of the Zr alloy rods for an accident tolerant fuel (ATF) cladding. The coating is expected to prevent or to slow down the reaction between the Zr alloy and steam at high temperature [3, 5]. It is known that such coatings should exhibit certain attributes, such as: excellent oxidation resistance, good thermal stability, high thermal conductivity, low neutron capture cross-section, and should be well-adhered to the Zr alloy substrate. To date, a few coatings (e.g. ZrN, Cr_2C_3, TiN, Al_3Ti, Cr, FeCrAl,) have been applied onto the surface of Zr alloys and studied in oxidising species environments [3, 6-9], showing the ability to reduce the oxidation speed of Zr alloys in air or steam to a certain extent. Nevertheless, the issue of durability in a high temperature steam environment has yet to be solved, which is one of the fundamental requirements for the design of a successful ATF cladding in the case of LOCA.

Metal nitride (MeN) coatings are known for their excellent oxidation resistance, good thermal stability, good resistance to erosion and low neutron capture cross-section [7, 10-13], and therefore are an ideal candidate for ATF applications. It has been reported that Si_3N_4 coating showed improved thermal stability and oxidation resistance over other MeN (Me=Zr, Ti, Al, Cr, Ta) coatings at high temperature in air environment [14]. The SiMeN (Si_3N_4/MeN, Me=Zr, Ti, Al, Cr, Ta) family of nanocomposite coatings consist of MeN nanoparticles dispersed in an amorphous Si_3N_4 matrix once the Si content is higher than $\sim$12 at%[14-16]. Such a nanocomposite structure enables the SiMeN coatings to provide excellent oxidation resistance, enhanced resistance to cracking, and higher hardness in comparison with MeN

coatings [14]. For instance, a nanocomposite coating consisting of TaN particles embedded in an amorphous Si_3N_4 matrix was found to be thermally stable in air up to 1300°C (heating up at 10°C/min, immediately cooling to ambient temperature once reaching 1300°C) [14]. As for the oxidation behaviour and degradation mechanism of Si_3N_4, extensive studies have been done, especially on bulk Si_3N_4. These studies have provided considerable insights into the underlying oxidation mechanisms. The oxidation of Si_3N_4 follows parabolic growth kinetics, which are controlled by the inward diffusion of oxidising species through the formed oxide scale [2, 17, 18]. When such thermally stable SiMeN (Si_3N_4/MeN, Me=Zr, Ti, Al, Cr, Ta) nitrides (with thicknesses of few micrometres) are applied as a protective coating for metallic substrates, e.g. Zr alloy, the nitrides coatings can degrade by cracking or spallation due to the thermal expansion mismatch between coating and substrate, but also can degrade by depletion of Si or Me (Me=Zr, Ti, Al, Cr, Ta), which are depleted by oxide scale formation and inward diffusion into the underlying substrate. To minimise the thermal expansion mismatch, inserting an interlayer between the substrate and the coating is expected to engineer a good interfacial performance between coating and substrate [19, 20]. For example, molybdenum (Mo), of which the coefficient of thermal expansion is between that of Zr alloy ($6.0x10^{-6}K^{-1}$) and Si_3N_4 ($3.2x10^{-6}K^{-1}$) can alleviate the thermal mismatch [20-22]. As for depletion and interfacial interdiffusion or inter-reaction, the diffusion of elements from the underlying substrate into the top coating can degrade the composition or microstructure of the coating and the diffusion from the coating into the substrate can cause depletion of elements in the coating, thereby resulting in premature failure of the coating [15]. However, whether the degradation of amorphous SiMeN nitride coatings during thermal exposure is induced by the elements diffusing from the substrate into the coating or from the coating towards the substrate remains unclear. Especially, numerous studies have shown that the elemental

diffusion from the substrate into amorphous SiMeN coatings can stimulate the crystallization of the amorphous coating, and in turn, its oxidation via grain boundaries that serve as fast diffusion paths in crystalline materials [14, 15, 23-25]. Nevertheless, the crystallization mechanism of amorphous coatings have not been sufficiently studied or understood, and the oxidation mechanism of amorphous nitride coating only considers the effect of the amorphous or crystalline status, without the consideration of the elemental composition. It was also shown in our previous work that no observable oxide scale on SiAlN coating after hundreds of hours thermal exposure, which was attributed to its amorphous microstructure status [26]. Nevertheless, the effects of elemental composition of SiAlN, especially, Si and N, on the oxidation behaviour were unclear.

In this study, a 1.1 μm thick SiAlN amorphous coating consisting of AlN nanoparticles dispersed in an amorphous Si_3N_4 matrix, with a 300 nm or 750 nm Mo interlayer have been deposited on Zr alloys and studied in a steam environment at 1000°C. The effects of different thicknesses Mo interlayer on interfacial diffusion or inter-reaction, and thereby, the related composition variation of the amorphous SiAlN coatings upon thermal exposure have been examined. This work provides new insights into the oxidation and degradation of amorphous SiAlN coatings, with a focus on the effect of interfacial interdiffusion or inter-reaction on the elemental composition and microstructure of SiAlN.

2. Experiments

2.1 Sample preparation

The deposition of SiAlN coatings on Zr 2.5 wt% Nb alloy plates (～50 × 50 × 2 mm^3) were conducted in a Teer Coatings Ltd. UDP 350 sputtering system, reported in fine details

elsewhere [6]. Prior to deposition, the Zr alloy substrates were mechanically ground, polished and cleaned with acetone in an ultrasonic bath. Three vertically mounted magnetrons in a dimension of 300 x 100 mm^2, fitted with 99.5% commercial Si, Al and Mo targets, were assembled in opposed positions through the sputtering chamber walls. Inside the chamber, there was a centrally mounted, unheated rotating sample holder. Before coating deposition, the pressure inside the chamber was reduced to a value below $1x10^{-3}$ Pa. After that, the sputter cleaning on the surface of Zr alloy substrates was conducted at -600 V DC for 15 minutes. The Si, Al and Mo targets were attached to magnetrons that were run at applied powers of 700, 300 and 500 W, respectively, driven by Advanced Energy Pinnacle Plus power supply.. The pulse frequency was set to 100 kHz at 60% duty. The Zr alloy substrates were applied a DC bias of -30 V throughout the coating deposition. During the deposition of interlayer Mo, only Ar was introduced into the chamber ($\sim 2.1\times10^{-3}$ mbar). Following this, N_2 reactive gas was introduced to deposit SiAlN coating. During the deposition of SiAlN, the N_2 to Ar gas ratio was kept constant at 20:60 sccm, respectively, and was controlled using a mass flow controllers (MKS Ltd.). The working pressure was also monitored using Baratron pressure gauge and was kept at the range of $\sim 3.0\times10^{-3}$ mbar based on the previous nitride coating fabrication experience [6]. The substrate was placed on a rotatable holder rotating at the speed of 30 rpm throughout the deposition of Mo and SiAlN. The substrate temperature did not exceed 350^{o}C during sputtering at operating conditions used in this work. The deposition rates for Mo and SiAlN coating were about 15 nm/min and 9 nm/min, respectively.

2.2 Adhesion and oxidation tests

The adhesion of as-fabricated coatings with or without Mo interlayer to the Zr alloy substrate was evaluated using nano-scratch testing. A spheroconical diamond indenter with a tip radius

of 5 µm and a cone angle of 90° was applied to scratch the SiAlN coated surface. The applied normal load, ranging from 0 to 450 mN, was increased linearly. Simultaneously, the displacement into surface had been well monitored by the rig (Nanoindentor MTS Nanoindenter XP). For coatings having thicknesses of around 1 µm, the nano-scratch test showed relatively high reproducibility and low sensitivity to testing parameters, such as loading rate or stylus radius. The length of the scratch distance was 300 µm and a force of 50 µN was applied for the profiling load. Five scratches were made on each sample in order to determine the critical loads for adhesive failure. Two critical load parameters were used to rank the interfacial adhesion. The first critical load, Lc1, described the load at which the onset of edge cracking was observed. The second critical load, Lc2, described the load at which the first sporadic isolated adhesion failure took place [27].

Oxidation test in the steam environment was carried out by flowing Ar/water vapour mixture through a quartz tube inside the tube furnace (Carbolite, UK) at 1000°C for 1 h. Firstly, Ar at a flow rate of 0.4 L/min was poured through the flask filled with ~400 ml of boiling water. Then, the large amount of water vapour was carried by the flowing Ar to the hot zone of the furnace where the SiAlN-coated alloy plates were located. The volume of the water vapour passing over SiAlN-coated alloy plates was calculated to be 1.74 L/min. In order to minimise the effects of ramping and cooling processes, the SiAlN-coated alloy plates were placed directly in the hot zone of the furnace when the temperature reached 1000°C. After 1 hour exposure, the samples were retracted to an ambient temperature zone cooled in Ar inside the quartz tube away from the hot zone.

2.3 Microstructural characterisation

The surface and cross-section images of the as-deposited and oxidised samples were examined by scanning electron microscopy (SEM, FEI, Magellan 400 XHR and Quanta 650) and the focused ion beam (FIB, FEI, Helios 660 and Quanta 3D). To achieve high resolution images, samples were analysed using transmission electron microscopy (TEM, FEI, Tecnai G2 and Tecnai TF30). Prior to TEM analysis, thin lamellae were cut out of the cross-sections of the SiAlN samples by FIB using the lift-out technique. In order to obtain the compositional profile of N, Si and Al throughout the coating stack, the lamellae were examined by a Talos F200A coupled with a Super-X-EDS system. The identification of the reaction product between SiAlN coating and Zr alloy substrate was examined by a transmission Kikuchi diffraction (TKD) operated on an FEI Magellan 400 XHR. The TKD technique is particularly effective in studying materials with fine grains due to its high spatial resolution, described in detail elsewhere [28]. The Thermocalc 4.0 software was conducted to calculate the Gibbs reaction energy following the Calphad rules.

The as-deposited and oxidised SiAlN coatings were also analysed using focused ion beam -- X-ray photoelectron spectroscopy (FIB-XPS, AXIS Spura). This technique combining FIB and XPS was useful in analysing the elemental and chemical compositions as a function of depth across the thin film. The surface of SiAlN coated plate was depth sputtered using 5kV Ar+ ions to gradually mill away surface material. A 2 mm x 2 mm etch crater was milled and the central 110 µm area of the etch crater was analysed. Survey scans were acquired after each etching cycle and quantification was performed after background subtraction.

3. Results

3.1 As-deposited SiAlN coating

Fig. 1 shows the cross-sectional SEM micrographs of an as-deposited SiAlN coating without any interlayer (Fig. 1 a), with a 300 nm thick Mo interlayer (Fig. 1 b), and with a 750 nm thick Mo interlayer (Fig. 1 c), respectively. The SiAlN coatings show smooth, homogeneous and fully dense microstructures without any visible pores or cracks. The thicknesses of the SiAlN coatings are about 1.1 µm and the thickness measurements consider the tilt correction.

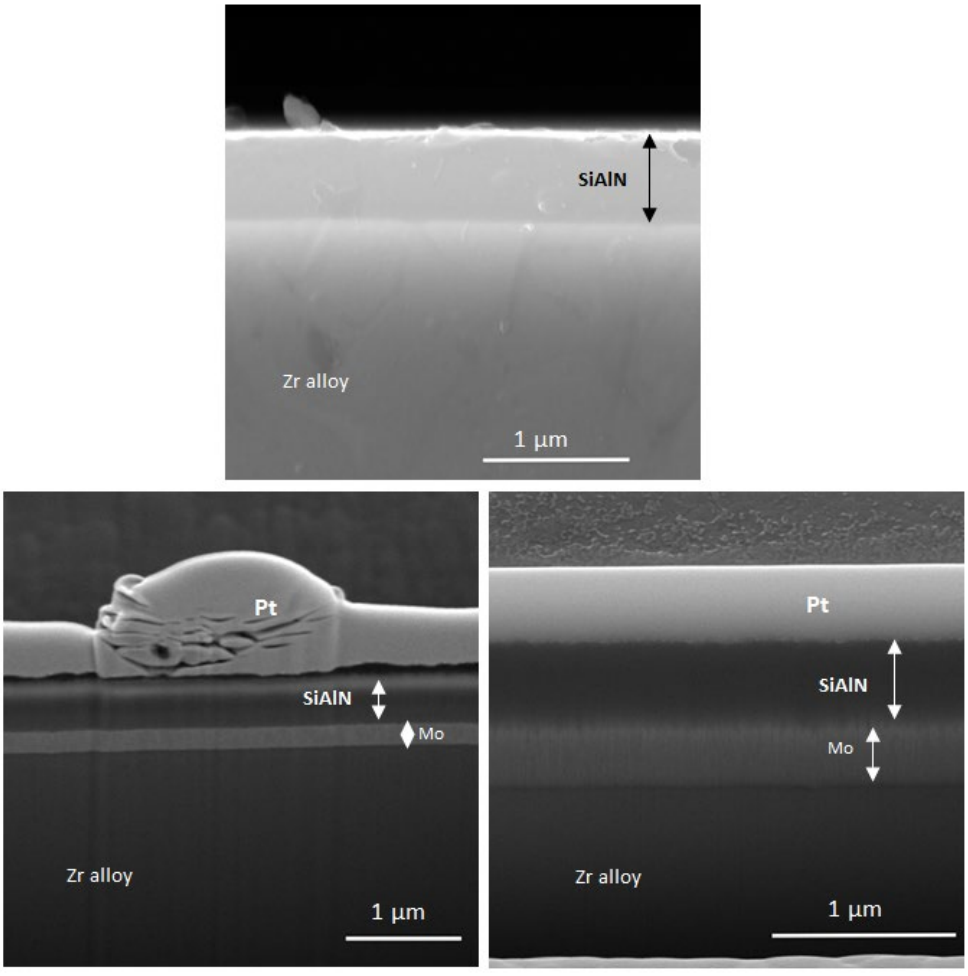

Fig. 1 Cross-sectional SEM images of as-deposited SiAlN coatings without or with Mo interlayers (a) without interlayer; (b) 300 nm Mo (tilting 52°, Pt layer for surface protection during FIB milling); (c) 750 nm Mo (tilting 52°, Pt layer for surface protection during FIB milling).

In order to investigate the microstructure and constituents of the SiAlN coatings in detail, TEM and XPS analyses were carried out. Fig. 2 a shows cross-sectional HAADF micrograph of an as-fabricated SiAlN coating with a 300 nm thick Mo interlayer. Again, the SiAlN coating is dense and smooth without any cracks or pores. The Mo interlayer (300 nm thick), deposited directly onto Zr alloy substrate, provides a well bond between the nitride coating and the substrate. The selective area diffraction (SAD) pattern (Fig. 2 a1) of the as-deposited SiAlN coating displays a diffraction halo, which indicates that the SiAlN is amorphous. Fig. 2 d exhibits SiAlN coating analysed by XPS showing an atomic concentration of the present elements as a function of milling time (depth). During each milling cycle, the surface of the SiAlN coating is removed by Ar+ ions and followed by the XPS analysis. The composition of the as-deposited SiAlN coating comprises of Si: ~40 at %, Al: ~8 at %, N: ~46 at% and some Ar contamination most likely from the sputtering gas or embedded during the XPS etching process. The Si, Al and N distributions throughout the SiAlN coating are consistent to a certain extent (in the out-of-plane direction). Such compositional analysis by XPS is also consistent with Super-X-EDS line analysis by TEM (not shown here). Based on the binding energy peak position fitting, the SiAlN coating is composed of Si_3N_4 and AlN [29-31]. It can be observed from HRTEM and FFT analysis (diffuse rings) shown in Fig. 2 b and b1 that the SiAlN coating is amorphous, including both AlN and Si_3N_4 phases. The dark AlN nanoparticles, marked by red circle line, disperse in the Si_3N_4 matrix, as displayed by HAADF image in Fig.2 c.

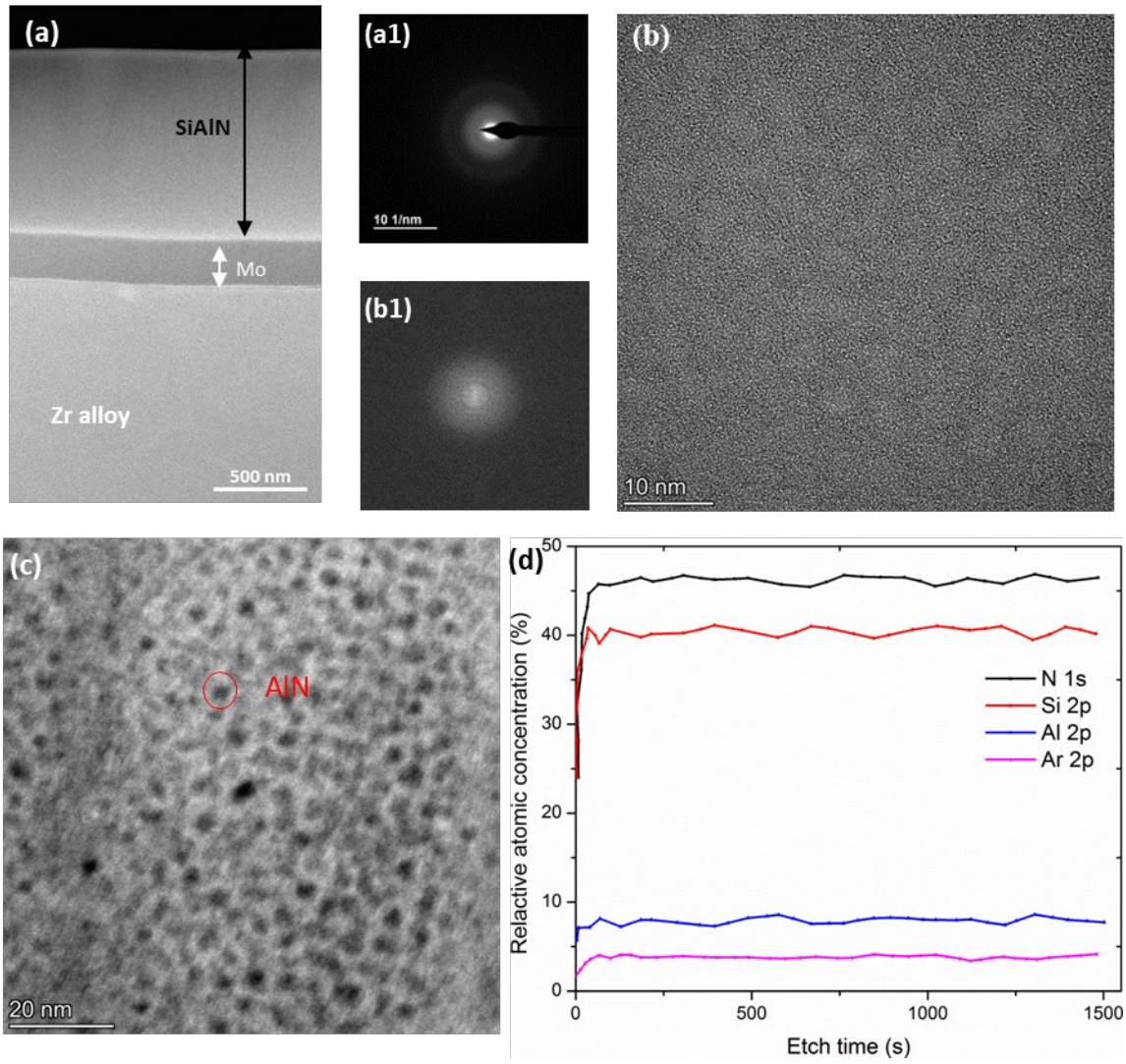

Fig. 2 (a) Cross-sectional HAADF image of as-deposited SiAlN coating with Mo 300 nm interlayer, (a1) is the selected diffraction pattern of the white box in (a); (b) Cross-sectional HRTEM image of as-deposited SiAlN coating, inset is the high magnification image, (b1) is FFT spectra of (b); (c) Cross-sectional HAADF image of as-deposited SiAlN coating; (d) The XPS analysis of FIB milled as-deposited SiAlN coating.

3.2 Adhesion

In order to characterise and compare the adhesion of the SiAlN coatings (without or with Mo interlayers) to the Zr alloy substrate, scratch testing has been carried out. The scratch test is a semi-quantitative measurement of the coating/substrate adhesion by measuring the critical load [27]. Several authors have shown that continuing scratching leads to the gradual degradations described as: cohesive failure (cracks), local chipping or buckling of the coating,

and finally, delamination [27, 32]. Fig. 3 shows the SEM micrographs of scratch tracks on SiAlN coatings without or with Mo interlayers. The SiAlN coating without an interlayer has the lowest adhesion among the three coating systems. It is almost completely removed from the scratch track, and the normal critical load Lc2 is only 15±7 mN, as shown in Fig. 3 a. With a metallic Mo interlayer, the critical load Lc2 is increased. The normal critical load of SiAlN coatings with a 300 nm Mo and a 750 nm thick Mo interlayer are 135±8 mN and 140±10 mN, respectively. Furthermore, there is a limited amount of sporadic cohesive failure (cracks) at relatively high critical loads close to Lc2, as shown in Fig. 3 b and c. To conclude, the SiAlN coating without an interlayer shows poor adhesion to Zr alloy substrate, but there is a substantial increase in coating adhesion by adding a Mo metal interlayer, although the thickness of the interlayer has not significantly influenced the critical load in these tests.

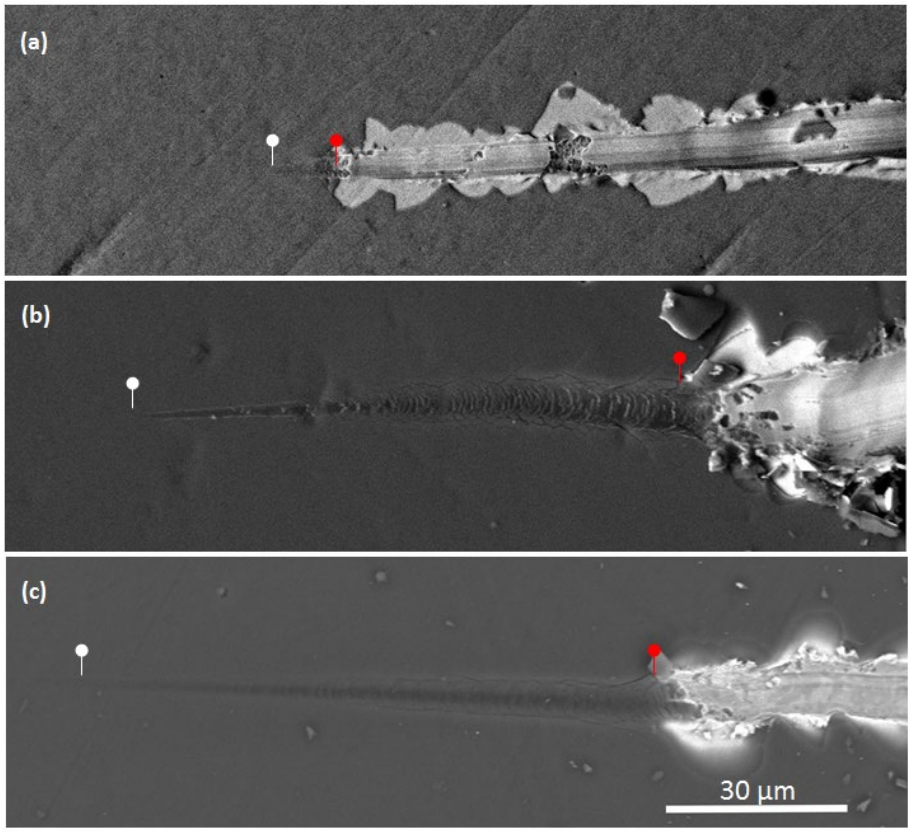

Fig. 3 SEM micrographs of scratch tracks of SiAlN coatings (a) without interlayer; (b) with 300 nm Mo interlayer; (c) with 750 nm Mo interlayer.

In order to study the intrinsic resistance of the SiAlN coatings to cracking and spallation during heating, high temperature dwelling and subsequent cooling, the SiAlN coatings (without or with Mo interlayers) were treated in a vacuum at 1000°C for 1 h. The vacuum treatment eliminated oxidation, and therefore, any material response observed after heat treatment was purely related to the intrinsic properties of the coatings or the substrate/coating interactions. Fig. 4 shows the top surface of the coatings in the as-deposited state (Fig.4 a-c) and after vacuum treatment (Fig. 4 a1-c1) with different interlayers. After this treatment, there are some cracks on the SiAlN coating without an interlayer, which can be explained by different thermal expansion coefficients between SiAlN and the Zr alloy (see Table 1) [20-22, 33-37]. However, there is no spallation or cracking on SiAlN coatings with Mo interlayers after vacuum treatment, as shown in Fig. 4 b1 and c1. This can be attributed to the fact that the Mo interlayer relieves the thermal stress between the substrate and coating as the coefficient of thermal expansion of Mo is between those of SiAlN and Zr alloy, as shown in Table 1.

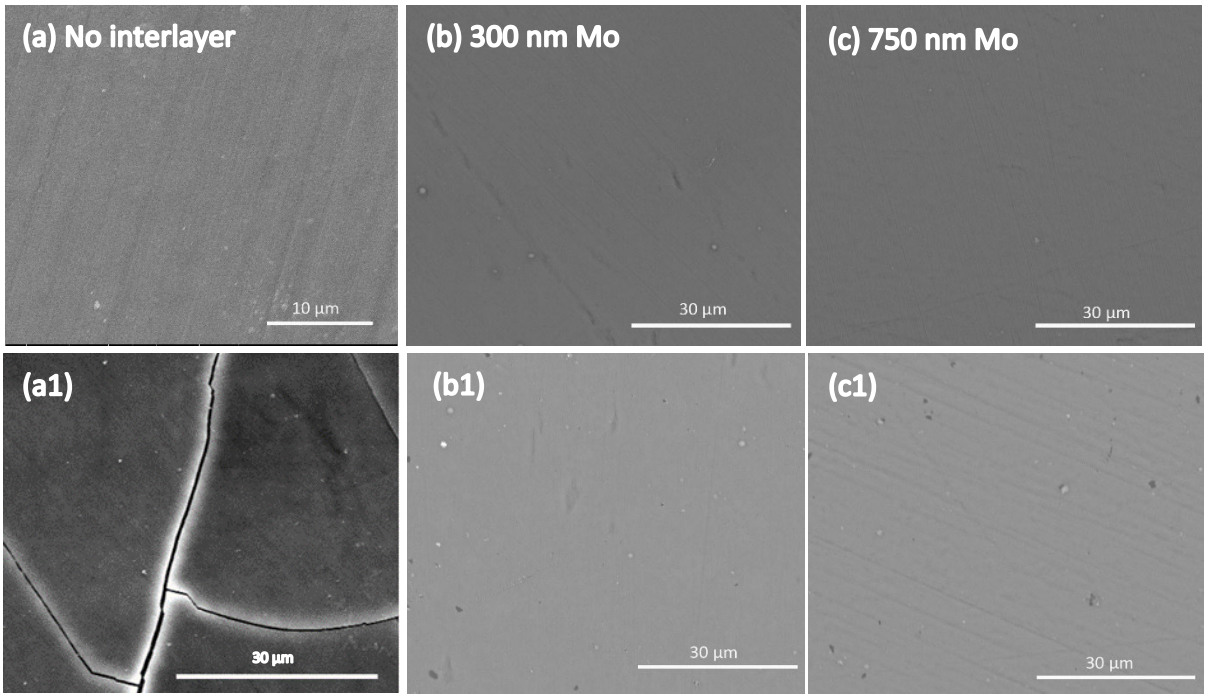

Fig. 4 The top surface of as-deposited and after vacuum treatment at 1000°C for 1 h of SiAlN coatings without or with Mo interlayers. SiAlN coating without interlayer: (a) as-deposited, (a1) 1000°C vacuum for 1 h; SiAlN coating with 300 nm Mo: (b) as-deposited, (b1) 1000°C vacuum for 1 h; SiAlN coating with 750 nm Mo: (c) as-deposited, (c1) 1000°C vacuum for 1 h.

Table 1: Compilation of the interlayer, substrate and coating, and some of their properties [20-22, 33-37].

Material	**Coefficient of thermal expansion ($x10^{-6}$ K^{-1})**
Mo	5.0
Si_3N_4	3.2
ZrNb	6.0
Zr_3Si_2	8.11
Zr_2Si	7.0
Zr(Mo)	~6.0
Mo_3Si	7.0
SiO_2	2.5
Al_2O_3	5.5

3.3 Oxidation behavior

Fig. 5 a-c show the cross-sectional microstructure of SiAlN coatings without Mo, with 300 nm and 750 nm thick Mo interlayers, respectively, after steam oxidation at 1000°C for 1 h. Severe cracking and oxidation have occured in the Zr alloy protected by SiAlN coating without Mo interlayer, as shown in Fig. 5 a and a1. For the SiAlN coating with a 300 nm thick Mo interlayer, an oxide layer with a thickness of 150 nm was observed on the top surface; whereas for the SiAlN coating with a 750 nm thick Mo interlayer, no oxide layer was identified under the SEM. No cracking or spallation was observed in the coatings with different thicknesses of Mo interlayer (Fig. 5 b/b1 and c/c1). Thus, the SiAlN coatings with 300 nm or 750 nm Mo interlayers can provide a good protection for Zr alloys against steam oxidation at 1000°C for 1 h; while the bare alloy can form an oxide scale with a thickness of 21 µm (measured on the

back side of the sample without coating) in identical conditions. However, it seems that interdiffusion between the Mo interlayer and Zr alloy substrate has occurred in both cases after high temperature of oxidation. The 300 nm thick Mo interlayer completely diffuses into the underlying Zr alloy, whreas in case of the 750 nm thick Mo the layer has decreased to about 500 nm this phenomenon will be further discussed below.

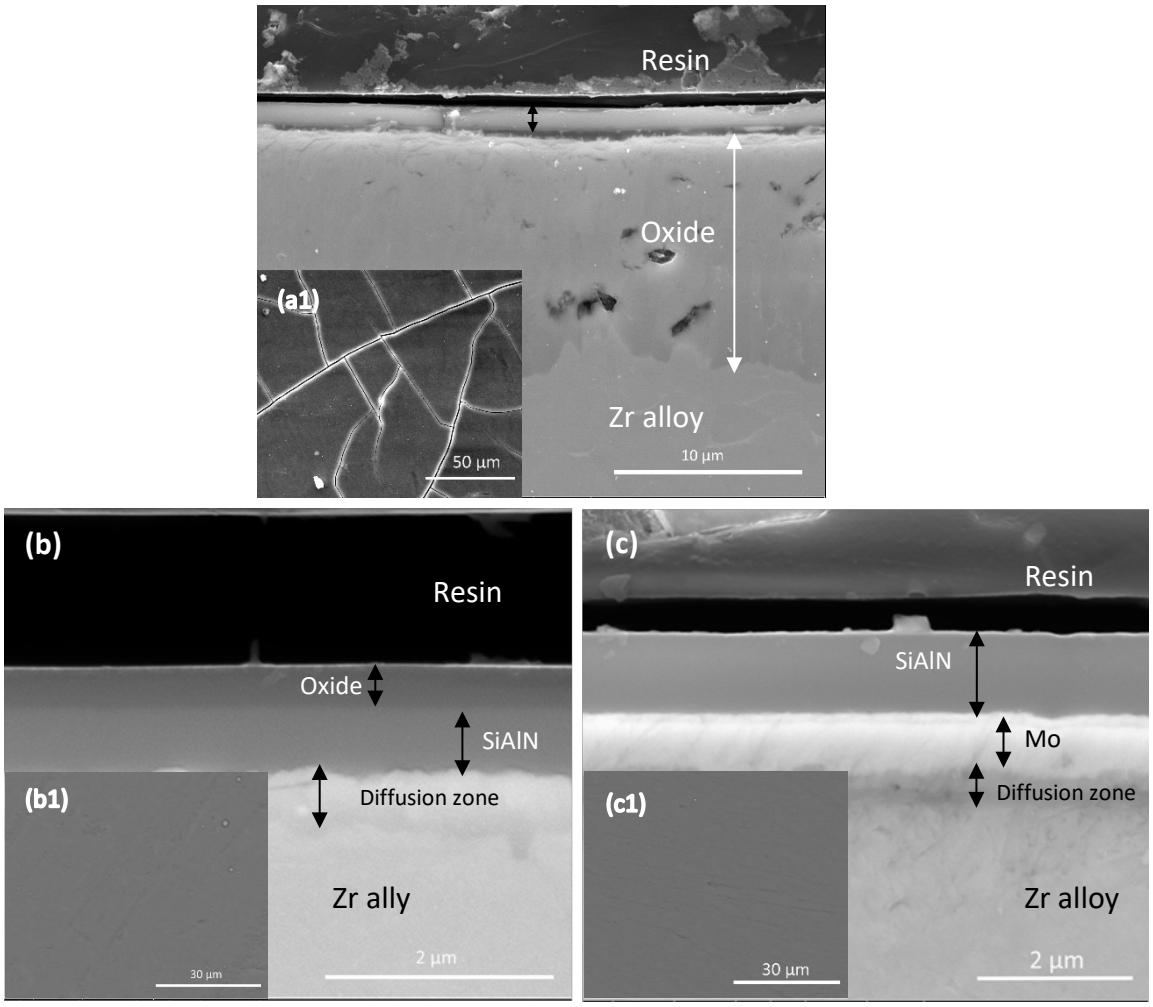

Fig. 5 Cross-sectional and top surface SEM images of SiAlN coating after oxidation at 1000°C steam for 1 h. (a) and (a1) without Mo interlayer; (b) and (b1) with 300 nm Mo interlayer; (c) and (c1) with 750 nm Mo interlayer.

In order to obtain greater details on the microstructure of the oxidised coatings and the interdiffusion between the Mo interlayer and Zr alloy substrate, thin lamellas from the cross-sections of the coatings were prepared by FIB using the lift-out technique and then analysed

by TEM. Fig.6 a and b show the cross-sectional BF STEM micrograph and corresponding EDS-STEM elemental maps of the SiAlN coating with a 300 nm thick Mo interlayer after steam oxidation at 1000°C for 1 h. It is observed that there is an oxide layer with a thickness of about 150 nm on top of the SiAlN coating after steam oxidation and the thin oxide layer is dense, crack free and pore free. The oxide mainly consists of SiO_2 and Al_2O_3, as confirmed by XPS analysis shown in Fig. 7. Moreover, de-convoluted high resolution XPS spectra obtained from N 1s suggest that borh Si and Al form oxi-nitrodes alongside alumina and silica [38, 39], which is confirmed by Si oxi-nitride phase at Si 2p at 102.7 eV [38]. There is also Al-OH phase detected in Al 2p peak shifted to higher binding energies (76.5 eV) [40], however since there are no characterists peaks for silicates detected from O 1s or Si 2p high resolution spectra (i.e. both shifted to higher binding energies) [41], therefore it is believed that the amount of Al-OH phased is rather insignificant and apears only on the coating surface. The remnant SiAlN coating (~700 nm thick) in contact with thin oxide remains integral and dense. The 300 nm thick Mo interlayer, completely diffuses into the Zr alloy after oxidation at 1000°C, as shown in the STEM image and EDS map of Mo (Fig. 6 a and b). Without the Mo barrier layer, the Zr substrate can react with SiAlN at 1000°C, and then the interface has transformed into a zirconium silicon intermetallic compound (Zr_2Si phase), as shown in red colour in the TKD analysis in Fig.6 c.

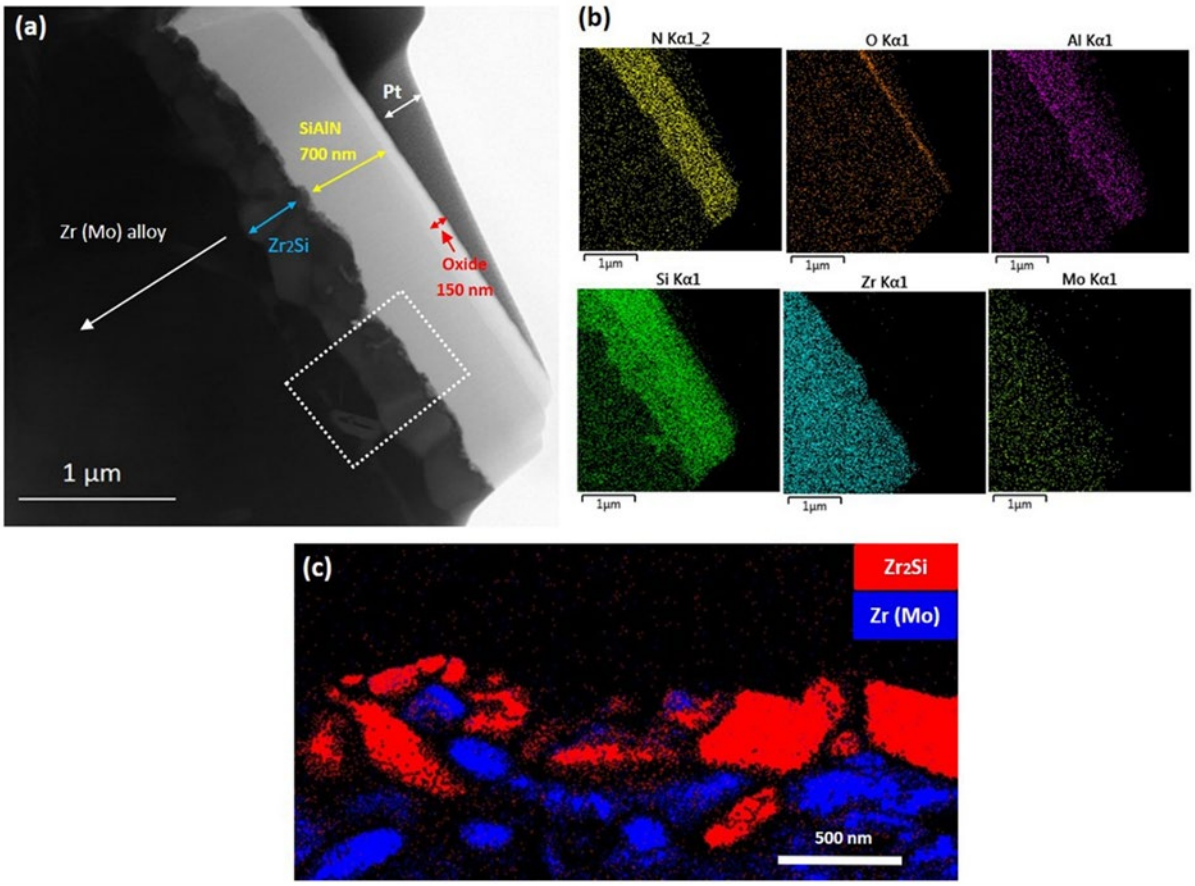

Fig. 6 (a) Cross-sectional BF STEM micrograph of SiAlN coating with 300 nm Mo after steam oxidation at 1000°C for 1 h; (b) the corresponding EDS-STEM elemental maps of Si, Al, N, O, Mo and Zr in (a); (c) TKD phase map of interface (Zr_2Si phase is shown in red colour, blue is Zr (Mo), white box area in (a) for TKD analysis).

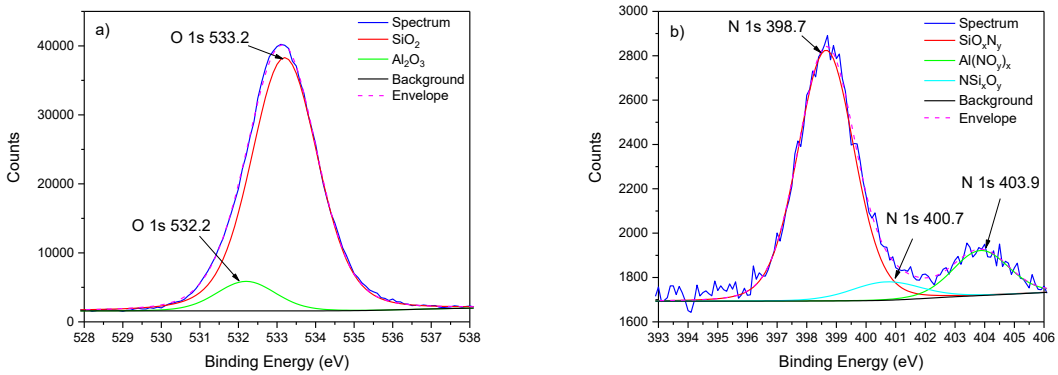

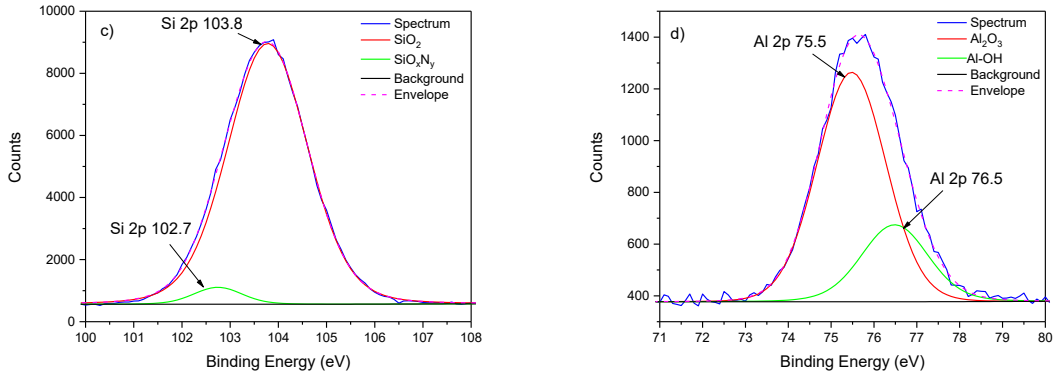

Fig. 7 XPS analysis of oxide formed on SiAlN coating surface with 300 nm Mo interlayer after oxidation at 1000°C for 1 h. (a) O 1s high resolution XPS spectra with the assigned atomic concentration of each de-convoluted phase. (b) N 1s high resolution XPS spectra with the assigned atomic concentration of each de-convoluted phase. (c) Si 2p XPS high resolution spectra and (d) Al 2p XPS high resolution XPS spectra.

After the thermal exposure, the interdiffusion and inter-reaction between the SiAlN/Mo coating and Zr alloy substrate may change the chemical composition and deteriorate the structure of the SiAlN, and thereby degrade the oxidation resistance of the coating. It had been reported that the diffusion elements from the underlying substrate to the coating can stimulate the crystallization of an amorphous nitride coating, and thereby promote the formation of oxide on the coating [15]. Fig. 8 shows the HRTEM analysis of the oxide and remnant SiAlN coating after steam oxidation at 1000°C for 1 h. The whole remnant SiAlN coating remains completely amorphous based on the HRTEM and inset images, as shown in Fig. 8 d and e. This indicates that even though the interdiffusion/inter-reaction between the SiAlN coating and Zr alloy substrate occurs, the SiAlN coating remains amorphous while an amorphous oxide scale (HRTEM and inset images in Fig. 8 b and c) was formed after high temperature steam oxidation. The results are inconsistent with previous studies that have claimed that diffusion elements from the underlying substrate into an amorphous Si_3N_4/MeN(Me=Ti, Al, Zr, etc.) coating can stimulate crystallization of the coating, and thereby,

causes oxide scale formation on the crystalized coating [14, 15, 23, 24]. Again, this will be discussed in more detail later.

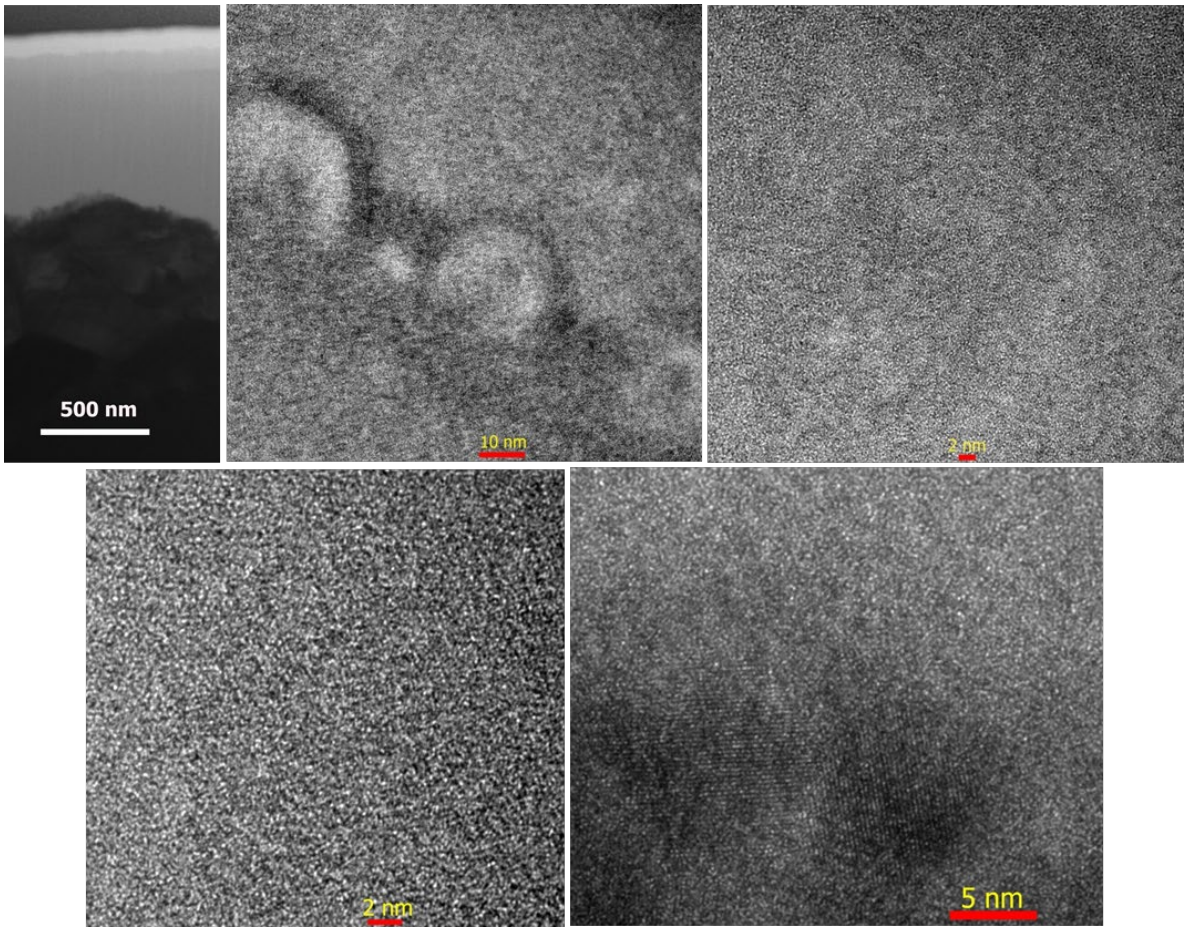

Fig. 8 HRTEM analysis of SiAlN coating with 300 nm Mo interlayer after steam oxidation at 1000°C for 1 h. (a) Cross-sectional STEM micrograph of SiAlN coating; (b) HRTEM image of interface between oxide and SiAlN coating (yellow box in (a)), insets are corresponding FFT. (c) HRTEM image of oxide scale (green spot in (a)), inset is the corresponding FFT. (d) HRTEM image of remnant SiAlN (orange spot in (a)), inset is the corresponding FFT. (e) HRTEM image of interface between SiAlN coating and underlying Zr_2Si layer (red box in (a)).

Fig. 9 a and b shows the cross-sectional BF STEM images of a SiAlN coating with a 750 nm Mo interlayer after steam oxidation at 1000°C for 1 h, together with the corresponding EDS elemental maps of N, O, Mo and Zr. After steam oxidation at 1000°C for 1 h, there is no observable oxide layer formed on the SiAlN coating although the Mo interlayer has been reduced from 750 nm thick to 500 nm due to interdiffusion between the Mo and Zr alloy

substrate, as shown in Fig. 9 a and b. The Zr from the substrate does not diffuse upwards into the SiAlN coating. Instead, the elemental Si from the SiAlN diffuses downwards through the Mo interlayer to the Mo/Zr alloy interface and thereby reacts with Zr forming a thin Zr_2Si layer. The diffusion of Si from SiAlN into the underlying substrate has caused a decrease in thickness of the SiAlN coating from the as-deposited value of 1.1 µm to about 1.0 µm. Even though there is downward diffusion of Si, the remnant SiAlN coating still remains an amorphous structure confirmed by the diffraction halo of the selective diffraction pattern for the SiAlN coating and HRTEM image with inset FFT image, as shown in Fig. 9 a and c, respectively.

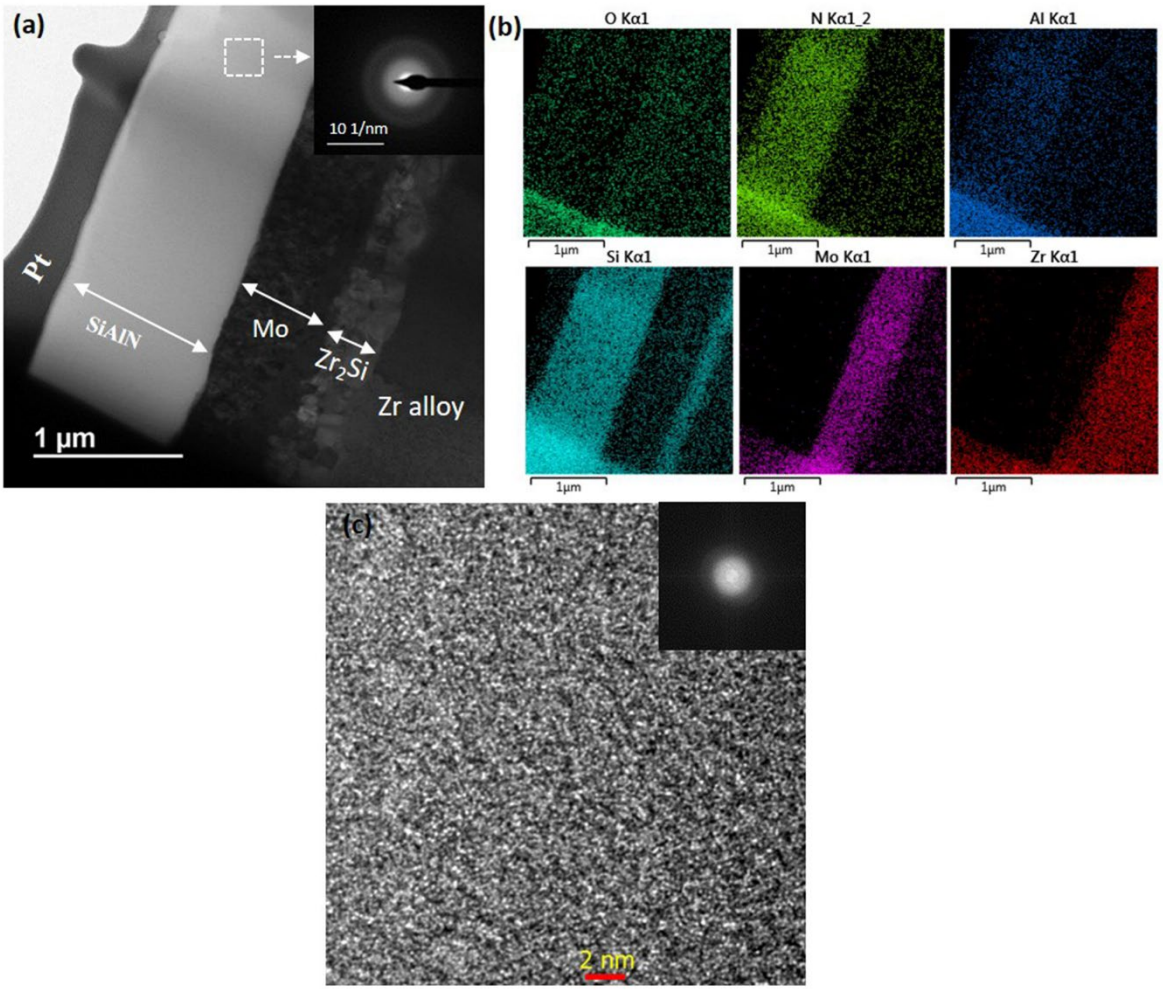

Fig. 9 (a) Cross-sectional BF STEM images of SiAlN coating with 750 nm Mo after steam oxidation at 1000°C for 1 h, inset is the SAD of white box. (b) The corresponding EDS-STEM elemental maps in (a); (c) HRTEM image of remnant SiAlN, inset is the corresponding FFT.

3.4 Compositional gradient of SiAlN coating after oxidation

Notably, whilst a thin oxide scale formed on the SiAlN amorphous coating with a 300 nm Mo interlayer, no oxide scale could be identified on the SiAlN amorphous coating with a thicker Mo diffusion barrier (750 nm) after steam oxidation at 1000°C for 1 h, as shown in Fig. 8 a and Fig. 9 a, respectively. In order to uncover the reasons for this difference, the composition of the SiAlN amorphous coatings with different thicknesses of Mo interlayer were characterized by HAADF coupled with Super-X-EDS in more detail after steam oxidation at 1000°C, as shown in Fig. 10 and Fig. 11. Fig. 10 shows the HAADF image and EDS line scanning of the SiAlN coating with a 300 nm Mo interlayer after steam oxidation at 1000°C for 1 h. A significant change in atomic fractions of Si and N in the remnant SiAlN compared with the as-deposited SiAlN condition is observed. The atomic fraction of N in the remnant SiAlN decreases from an as-deposited value of 46% to approximately 30% at a position close to the oxide/SiAlN interface whilst the atomic fraction of Si increases from an as-deposited value of 40% to about 55%. The atomic fraction of N exhibits a descending trend from the oxide/SiAlN coating interface to the coating/Zr_2Si layer interface. Conversely, the atomic fraction of Si shows an upward trend to about 60% at a position close to the coating/Zr_2Si layer interface. The atomic fraction of Al in the remnant SiAlN is about 8% to 10%, which is consistent with the as-deposited condition to some extent. The huge loss of N in the SiAlN coating may be the reason why there is a thin oxide scale on the SiAlN coating. In order to verify this assumption, the HAADF image and Super-X-EDS line analysis of the SiAlN coating without an observable oxide scale after steam oxidation at 1000°C for 1 h has been carried out, as shown in Fig. 11. At a position closest to the outermost surface of the SiAlN, the atomic fraction of N is about 45%, which is slightly lower than that of as-deposited SiAlN condition (46%).; and the atomic

fraction of Si is about 43%, which is slightly higher than 40% for the as-deposited condition. The atomic fraction of N also exhibits a descending trend from the approximately middle point of the remanent SiAlN coating to the coating/Mo interface while the atomic fraction of Si shows an upward trend to the underlying interface. It is noteworthy that the element Si in the SiAlN diffuses outwards to the underlying Mo interlayer and Zr alloy, confirmed by the Si counts′ line in Fig. 11 c. Some of the Si remains inside the Mo interlayer but most of the Si diffuses further to the underlying Zr alloy forming a Zr_2Si compound layer, as shown in the HAADF image in Fig. 11 a. It can be expected that the downward diffusion of Si in SiAlN may degrade the SiAlN coating and thereby results in the loss of N. There is no evidence that Mo or Zr diffuses upwards into the SiAlN coatings in the samples containing 300 nm or 750 nm thick Mo interlayer, as confirmed by Fig. 10 d and Fig. 11 d. For the coating with a 300 nm thick Mo interlayer, Mo completely diffuses into the Zr alloy; while for the 750 nm thick Mo, the layer reduces to 500 nm after oxidation at 1000°C for 1 h. For the 750 nm thick Mo interlayer, it may play a sluggish effect on the downward diffusion of Si and thereby contribute to the relatively high N fraction at the position closer to the outermost surface in the remnant SiAlN coating. The atomic fraction of Al in the remnant SiAlN is about 8% to 10%, which is consistent with the as-deposited condition to some extent.

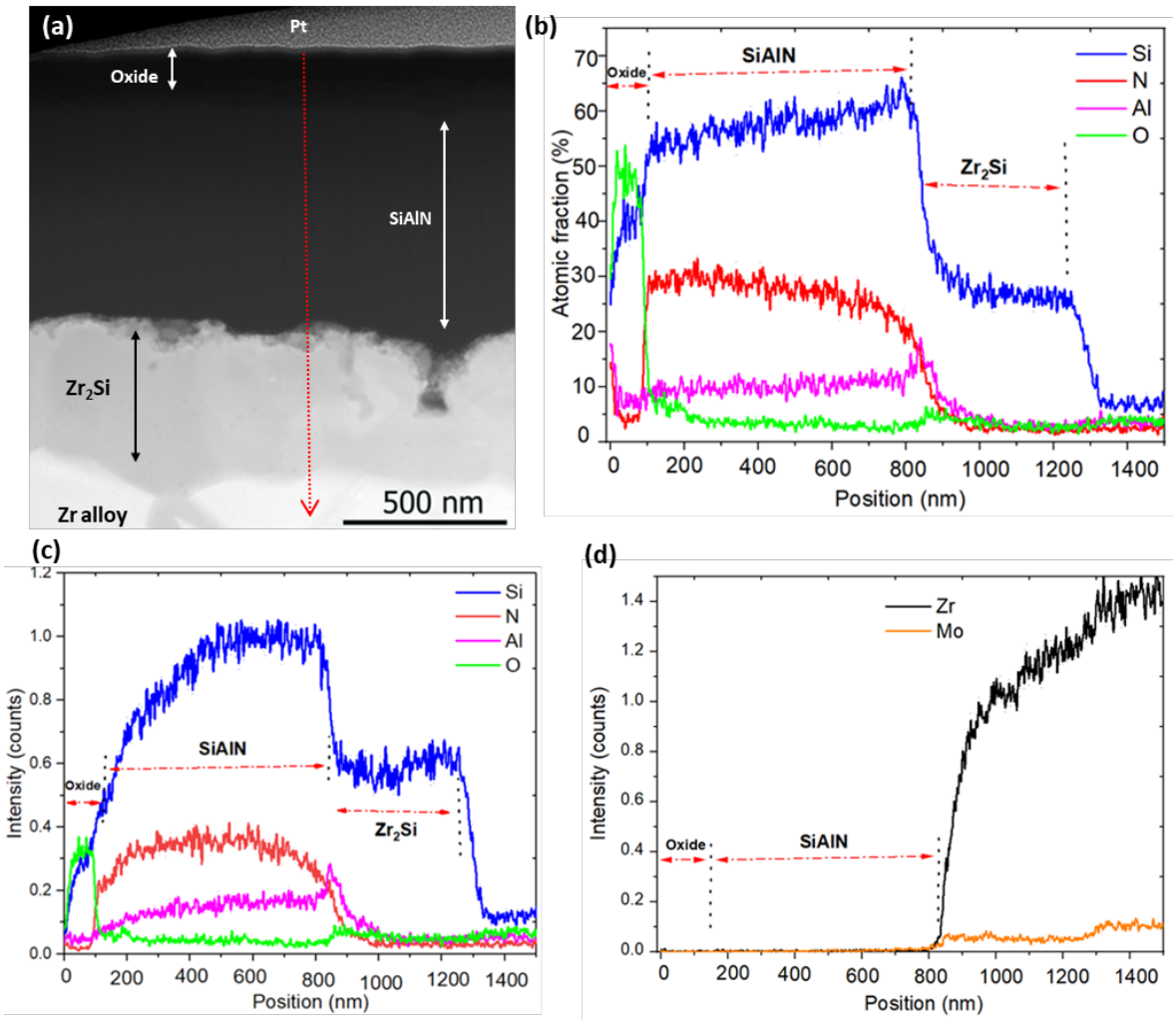

Fig. 10 (a) Cross-sectional HAADF image of SiAlN coating with 300 nm Mo after steam oxidation at 1000°C for 1 h. (b) EDS line scanning on atomic fractions of corresponding elements, following red line in (a). (c) EDS line scanning on counts of Si, Al, O and N elements, following red line in (a). (d) EDS line scanning on counts of Mo and Zr elements, following red line in (a).

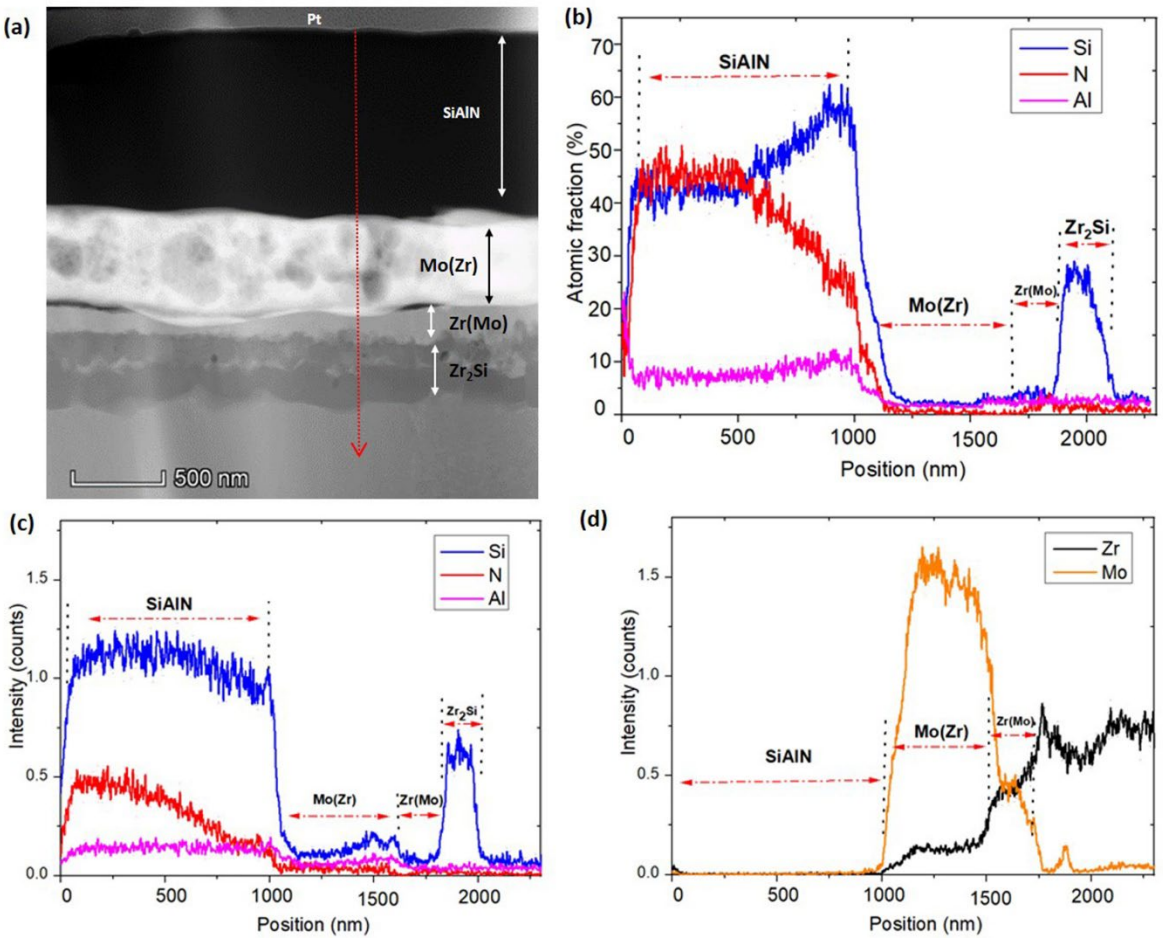

Fig. 11 (a) Cross-sectional HAADF image of SiAlN coating with 750 nm Mo after steam oxidation at 1000°C for 1 h. (b) EDS line scanning on atomic fractions of corresponding elements, following red line in (a). (c) EDS line scanning on counts of Si, Al and N elements, following red line in (a). (d) EDS line scanning on counts of Mo and Zr elements, following red line in (a).

4. Discussion

The findings in this work show that for identical SiAlN coatings, the thickness of the Mo interlayer has a substantial impact on the oxidation behaviour of the coating. A thin oxide scale forms on the SiAlN coating with a 300 nm Mo interlayer, while there is no evidence of oxide scale formation where the Mo interlayer is 750 nm thick. These findings suggest that the thicker Mo interlayer retards the reaction between SiAlN and the underlying Zr alloy substrate, playing a substantial role in the sluggish diffusion of the Si and N (downward) from the SiAlN coating, and thereby, retards the occurrence of oxidation, which in turn prolongs

the oxidation protection of the underlying substrate. Moreover, the degradation and oxidation mechanism of the amorphous nitride coating, which is inconsistent with previous studies [14, 15, 23-25], can be explained. The mechanistic interpretations of these findings will be explored in the following sections.

4.1 Downward diffusion of Si and N in SiAlN

Possible reactions between Zr, Mo and Si_3N_4 in SiAlN are listed as follows:

$$9Mo + Si_3N_4 = 3Mo_3Si + 2N_2 \qquad \Delta G(1273.15K) = -4.79x10^3\ J/mol \qquad (1)$$

$$Mo_3Si + 2Zr = 3Mo + Zr_2Si \qquad \Delta G(1273.15K) = -8.76x10^4\ J/mol \qquad (2)$$

$$6Zr + Si_3N_4 = 3Zr_2Si + 2N_2 \qquad \Delta G(1273.15K) = -2.67x10^5\ J/mol \qquad (3)$$

Among the 3 reactions, the most thermodynamic favourable reaction is reaction 3, the least favourable reaction is reaction 2, therefore, with the presence of Mo layer, Mo reacts with Si_3N_4 (the SiAlN coating consists of Si_3N_4 and a trace amount of AlN) at the Mo/SiAlN interface, forming Mo_3Si and N_2, as shown in equation 1. Then Mo_3Si reacts with Zr, forming a Zr_2Si phase validated by TKD analysis (Fig.6 c), as shown in equation 2. Once the Zr diffuses to the interface of the SiAlN, it can directly react with Si_3N_4, forming a Zr_2Si phase and N_2, as shown in equation 3. Such interfacial reactions cause depletion of Si in the SiAlN close to the interface between SiAlN and the underlying interlayer. Simultaneously, the Si from the outermost SiAlN diffuses downwards to the SiAlN/underlying interlayer interface. Thus, the interfacial reaction and diffusion of Si lead to compositional gradient across the SiAlN coatings after thermal exposure. The Mo layer, particularly with the thickness of 750 nm, can serve as a diffusion/reaction barrier between the SiAlN coating and Zr alloy substrate, thereby retarding

the downward diffusion of Si in the SiAlN, which in turn reduces the composition change of SiAlN, as shown by the schematic diagrams in Fig. 12. In Fig.12, (a) and (d) show theare as-deposited conditions, b and e show the transition conditions (thermal exposure process), and c and f are conditions after the thermal exposure in samples with 300 and 750 nm thick Mo interfaces, respectively. During the thermal exposure, both diffusional processes described above occur, while the thicker Mo layer could retard such reactions.

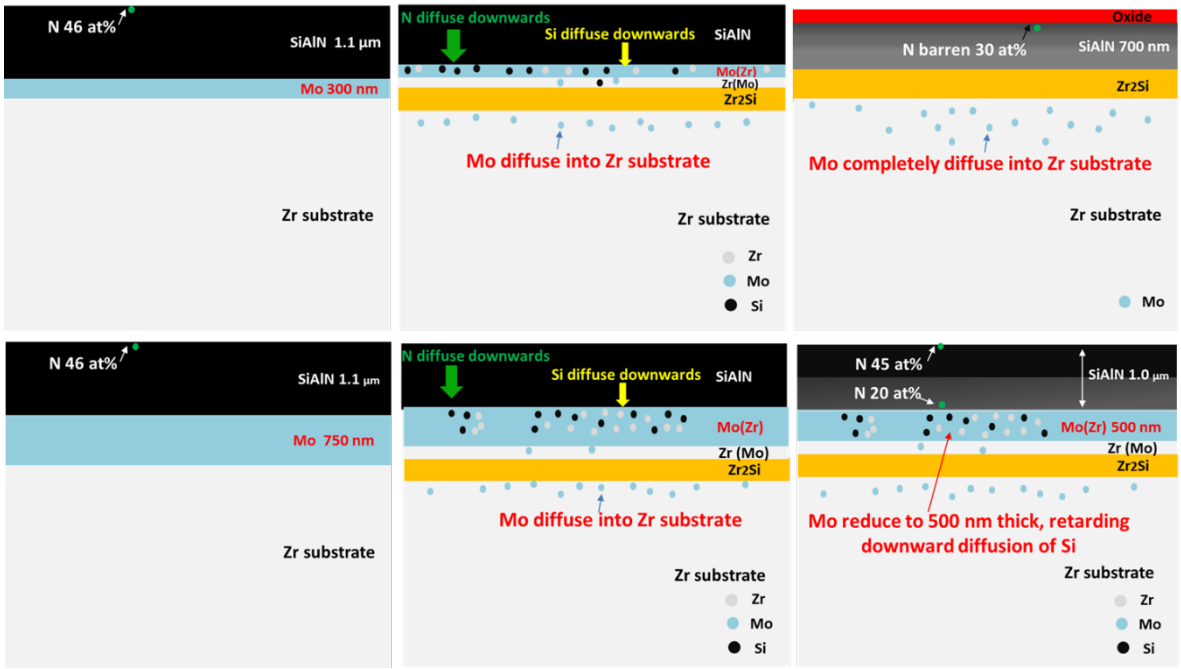

Fig. 12 Schematic diagrams of downward diffusion of Mo, Si and N in the SiAlN coating with 300 nm or 750 nm Mo interlayer during thermal exposure. (a-c) SiAlN with 300 nm Mo: (a) as-deposited condition, (b) thermal exposure condition, (c) after thermal exposure. (d-f) SiAlN with 750 nm Mo: (a) as-deposited condition, (b) thermal exposure condition, (c) after thermal exposure.

The N from the decomposed Si_3N_4 diffuses towards the underlying interlayer and the substrate via vacancies, as shown in Fig. 12 [42]. In general, nitrogen diffuses significantly faster than metal atoms, e.g. Si [42, 43]. The downward diffusion of N across SiAlN is faster than the downward diffusion of Si in the SiAlN coating, causing substantial loss of N, and thereby forms the relatively lower N atomic fraction in the SiAlN coating after the thermal

exposure. Moreover, the N diffusivity decreases with increasing N concentration [42]. The diffusivity of N gradually decreases from the position closest to the SiAlN/interlayer interface to the outermost surface, which causes a compositional gradient of N across the SiAlN coating after the thermal exposure, as shown in Fig. 12. During the downward diffusion of N, there is no observable nitride inside the underlying interlayer or Zr alloy substrate, due to the negligible content of N inside the interlayer or Zr alloy (Fig. 10 b and Fig.11 b-c), which is below its maximum solubility [44]. The diffusion rates of N are relatively fast in the interlayer or Zr alloy at 1000°C, and N could diffuse downwards far away from the interface [45, 46]. The solution of N in the Zr alloy substrate has been reported to have a detrimental effect on the oxidation of Zr alloy, if the Zr alloy was exposed to steam or air oxidising environment without any protective coatings [47, 48]. However, it has been shown in this study that the underlying Zr alloy has been well protected by SiAlN/Mo coatings and only a minimal amount of N has been detected in the underlying Zr alloy. Nevertheless, it is important to further investigate the inward diffusion mechanism of N.

4.2 Oxidation mechanism of amorphous SiAlN

At the surface of amorphous SiAlN coatings, the downward diffusion of Si and N cause the formation of nonstoichiometric SiNx with excessive Si and lean N after the thermal exposure, as discussed above. It was reported that amorphous SiNx films with a N content below 20 at% exhibited the formation of a Si phase after annealing to 900°C for 2 h [49]. Between 20 to 30 at% of N enables the formation of a Si phase after the heat treatment under a relatively higher temperature (1200°C) due to the N losses related to the fact that the thermally activated diffusivity of N decreases with increasing N concentration [42, 49, 50]. Thus, the outermost surface of the SiAlN coating (containing 300 nm thick Mo interlayer) with a composition: Si:

55 at%, Al: 10 at%, N: 30 at% (Fig. 9 b), has a strong possibility of forming a Si phase prior to oxidation at 1000°C. In order to verify such an assumption, the FIB-XPS was ideally suited to characterise the elemental and chemical composition of thin film throughout the coating thickness. The Si_{2p}-Si_{2p} bond has been observed in the remnant SiAlN closest to SiAlN/oxide interface of the SiAlN coating with a 300 nm Mo interlayer after oxidation at 1000°C for 1 h, while there was no observable Si_{2p}-Si_{2p} bond in the outermost surface of the SiAlN coating with a 750 nm Mo interlayer after identical treatment, as shown in Fig. 13 b and d. Thermodynamically, the Si, Si_3N_4 and AlN as shown in equations 4, 5 and 6 respectively, can react with water at 1000°C. However, the oxidation activation energy of Si is about 1/2 to 1/3 times that of Si_3N_4 in oxygen oxidising environments from 1000°C to 1400°C [17, 18]. Moreover, the parabolic rate constants for oxidation of Si are orders of magnitude higher than that for Si_3N_4. In high temperature water vapour environments, the H_2O molecules chemically dissociate into OH- and H+ and these ions can be absorbed by the SiAlN coating surface, and the O-H bonds can be further broken to free O ions [51]. Thus, the outermost surface of the SiAlN coating (with 300 nm Mo interlayer) with a Si_{2p}-Si_{2p} bond, can easily form a thin oxide scale after oxidation at 1000°C. Once a thin oxide scale is formed, the oxidation of SiAlN is controlled by the diffusion of O ions or OH- through the oxide scale towards the nitride/oxide scale interface. It has been widely reported that SiC or Si_3N_4 could react with water vapour to form a SiO_2, and SiO_2 scales also react with water vapour to form a volatile $Si(OH)_4$ species at relatively high temperature. The severe volatilisation of silica formers in water vapour environment happens at the temperature range above 1200°C [52-54]. At 1000°C, the possibility of SiO_2 scale formed on SiC volatility had been assumed to be negligible due to the lower relative volatilisation rate, and no observable volatilisation of silica formed on SiC in steam had been reported by Hay and Cao [55, 56]. Therefore, in our study on SiAlN

coatings exposed to steam at 1000°C for 1 h, the volatilisation of silica would be negligible. Also, no observable erode or volatilisation of silica morphology have been observed based on the top surface and cross section morphology of SiAlN coating with 300 nm Mo after oxidation, as shown in Fig. 5 a and inset.

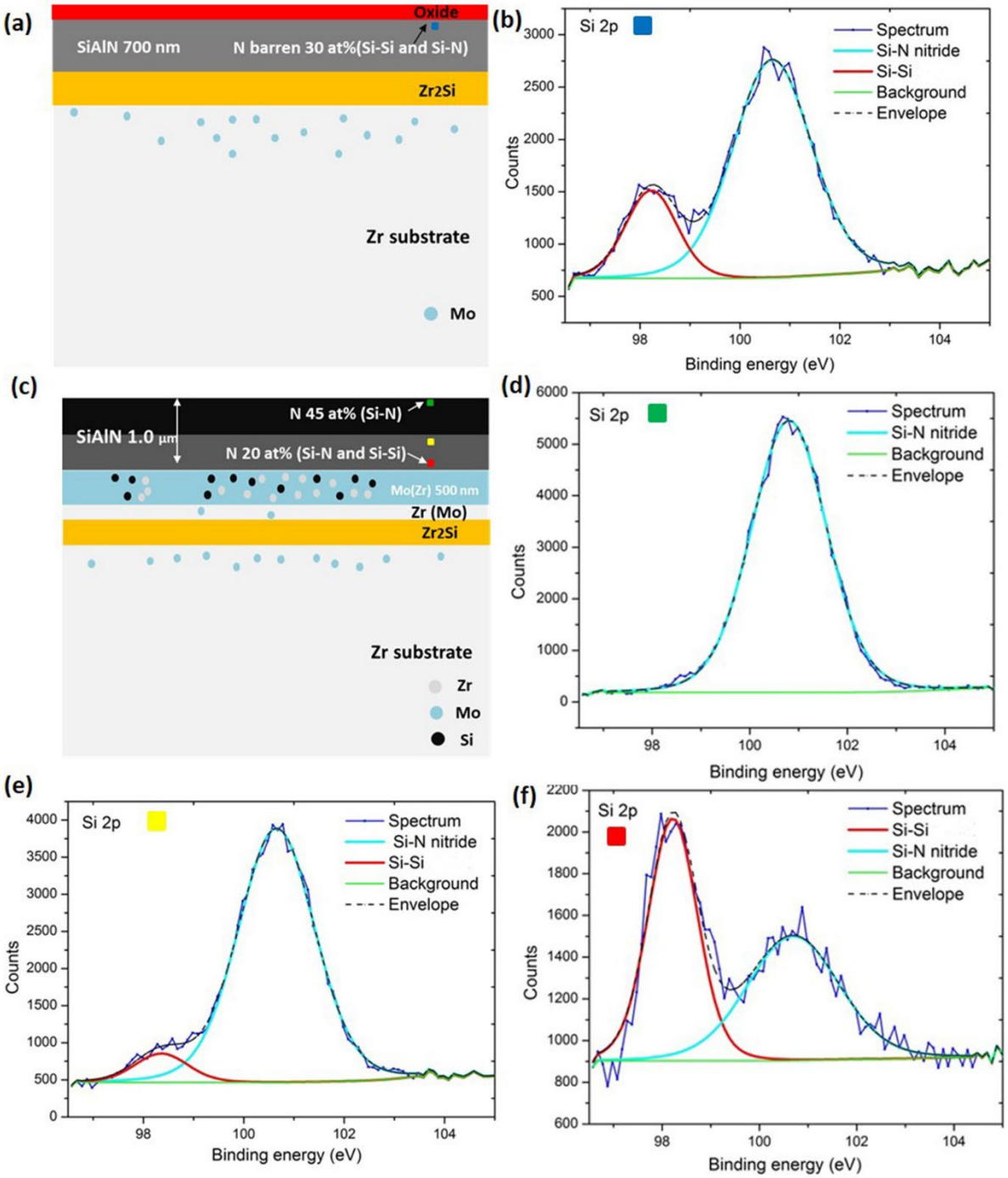

Fig. 13 FIB-XPS analysis on SiAlN coating with 300 nm or 750 nm Mo interlayer after oxidation at 1000°C for 1 h. (a) Schematic diagram of SiAlN coating with 300 nm Mo after oxidation; (b) Si 2p XPS spectra of SiAlN, acquired from the position close to SiAlN/oxide interface, blue rectangular box in (a). (c) Schematic diagram of SiAlN coating with 750 nm Mo after oxidation; (d) Si 2p XPS spectra of SiAlN, acquired from the position close to outermost surface of SiAlN, green rectangular box in (c). (e) Si 2p XPS spectra of SiAlN, acquired from the position ~400 nm to SiAlN/Mo interface, yellow rectangular box in (c); (f) Si 2p XPS spectra of SiAlN, acquired from the position close to SiAlN/Mo interface, red rectangular box in (c).

In the SiAlN coating with a 750 nm thick Mo interlayer, the residual amount of N at the outermost surface of the SiAlN is still 45 at%, which is close to Si_3N_4, Si_{2p}-N, as shown in Fig. 13 c and d, leading to good oxidation resistance [17]. Noticeably, the XPS analysis as a function of depth in Fig. 13 c-f indicates that a Si_{2p}-Si_{2p} bond gradually appears in the SiAlN from the outermost surface to SiAlN/Mo interface, indicating that the thicker Mo (750 nm) interlayer can only retard the downward diffusion of Si instead of avoiding diffusion. Once the thermal duration time is long enough, especially when Mo completely diffuses into the underlying Zr alloy substrate, the outermost surface of the SiAlN coating will also exhibit the Si_{2p}-Si_{2p} bond and the oxidation will happen eventually, like in case of the coating with the 300 nm Mo interlayer. An extended oxidation duration of 2 h of SiAlN coating with 750 nm Mo interlayer shows a thin oxide scale formation, which further validates the discussed degradation mechanism, as shown in Fig. 14

$$Si_3N_4 + 6H_2O = 3SiO_2 + 2N_2 + 6H_2 \qquad \Delta G(1273.15K) = -2.637 \times 10^5 \text{ J/mol} \qquad (4)$$

$$Si + 2H_2O = SiO_2 + 2H_2 \qquad \Delta G(1273.15K) = -3.28 \times 10^5 \text{ J/mol} \qquad (5)$$

$$2AlN + 3H_2O = Al_2O_3 + N_2 + 3H_2 \qquad \Delta G(1273.15K) = -1.916 \times 10^5 \text{ J/mol} \qquad (6)$$

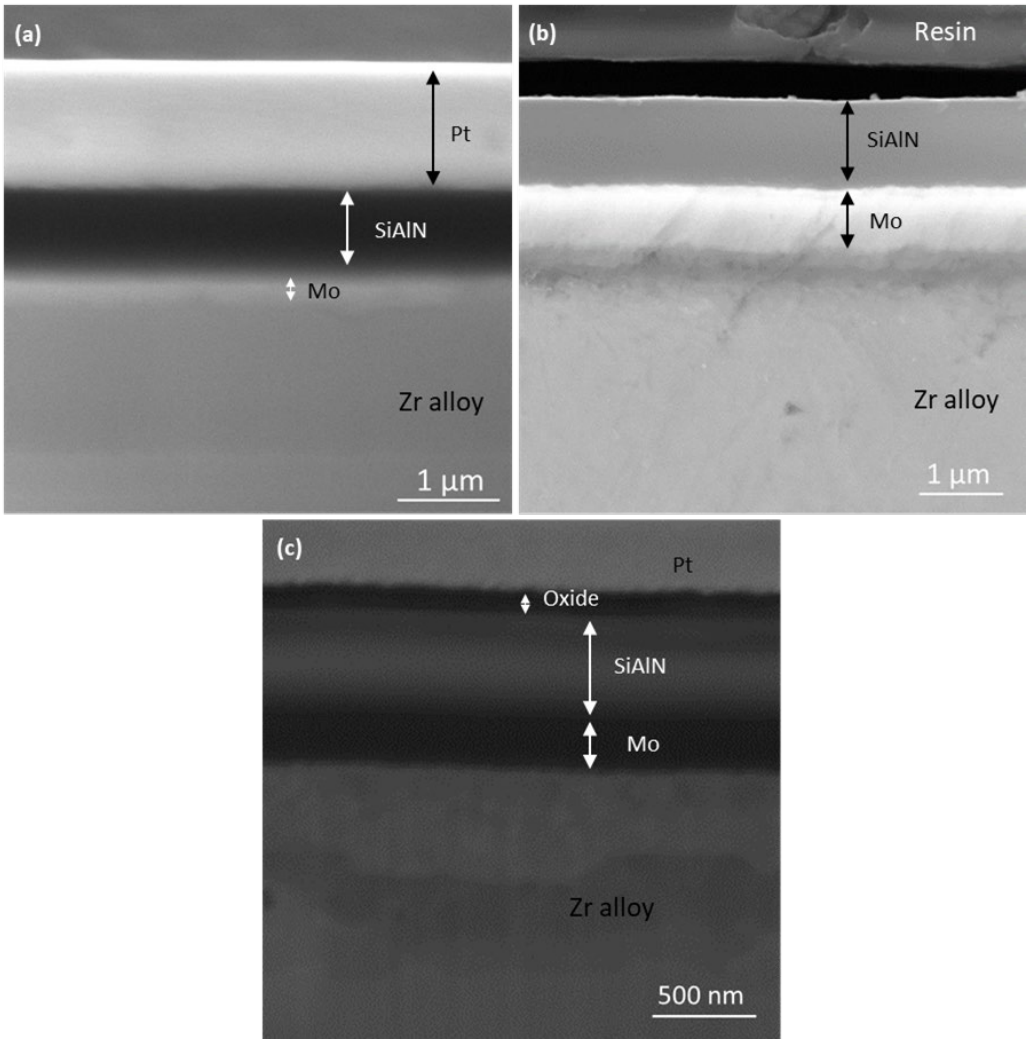

Fig. 14 Cross-sectional SEM images of SiAlN/Mo coating after oxidation at 1000°C steam for different duraction. (a) SiAlN/300 nm Mo interlayer for 0.5 h (tilting 52°, Pt layer for surface protection during FIB milling); (b) SiAlN/750 nm Mo interlayer for 0.5 h and (c) for 2 h (tilting 52°).

As for the effect of the microstructure status (u.e. amorphous or crystalline) on the oxidation resistance, the findings from previous studies suggest that the oxidation only happens on crystalline Si_3N_4 transformed from an amorphous condition [14, 15, 23-25], which is not supported by the present study. Actually, the comparisons of the oxidation behaviour between crystalline Si_3N_4 and amorphous Si_3N_4 have been widely reported and concluded that both structures exhibited excellent oxidation resistance at high temperatures in oxidising species. The activation energy of crystalline Si_3N_4 is slightly lower than that of the amorphous

form and the parabolic rate constant of crystalline Si_3N_4 is about three to four times larger than that of amorphous Si_3N_4 in dry oxygen, air or wet oxygen from 1000°C to 1600°C while the paraboli rate constant of oxidation of Si has orders of magnitude higher than that of Si_3N_4 [17, 18]. Thus, the oxidation of amorphous nitride coating is determined by elemental composition change instead of the widely reported amorphous or crystalline structure.

5. Conclusion

A series of 1.1 µm thick SiAlN amorphous coatings consisting of AlN nanoparticles dispersed in an amorphous Si_3N_4 matrix, with 300 nm or 750 nm Mo interlayers have been deposited on Zr alloy and studied in an oxidising environment. The following conclusions can be drawn from this work:

1. The SiAlN amorphous coating with 300 nm Mo interlayer forms an oxide scale, consisting of SiO_2+ Al_2O_3, after steam oxidation at 1000°C for 1 h, while there is no evidence of oxide scale formation where the Mo interlayer is 750 nm thick. The downward diffusion of Si into the underlying Zr alloy followed by the relatively faster downward diffusion of N generates excessive Si and lean N in the outermost surface of the SiAlN, forming Si-Si bond and depletion of N below 30% in the outermost surface, thereby resulting in the oxidation of the amorphous coating.
2. The thicker Mo interlayer (750 nm) taking advantage of retarding the reaction between SiAlN and underlying Zr, therefore plays a substantial role on the sluggish downward diffusion of Si and N from the SiAlN coating. This in turn retards the occurrence of oxidation and prolongs the oxidation protection of the underlying substrate.

3. This study uncovers the new insights into the coating design, suggesting that the prerequisite to acquire an excellent oxidation protection of Si_3N_4/MeN amorphous films is to mitigate the downward diffusion of Si, and thereby, mitigate or even avoide the oxidation of such amorphous films in oxidising environments at high temperature ranges. The oxidation mechanism of amorphous nitride coatings is determined by the elemental composition of the coating instead of the widely reported amorphous or crystalline status.

Acknowledgments

This work was supported by the appointment of Ping Xiao as Rolls-Royce/Royal Academy of Engineering Research Chair in Advanced Coating Technology since 2019. This work thanks the Henry Royce Institute for Advanced Materials, funded through EPSRC grants EP/ R00661X/1, EP/S019367/1, EP/P025021/1 and EP/P025498/1.

Reference

1. Zinkle, S.J. and G.S. Was, *Materials challenges in nuclear energy.* Acta Materialia, 2013. **61**(3): p. 735-758.

2. Robb, K.R., M.W. Francis, and L.J. Ott, *Insight from Fukushima Daiichi Unit 3 Investigations Using MELCOR.* Nuclear Technology, 2017. **186**(2): p. 145-160.

3. Terrani, K.A., *Accident tolerant fuel cladding development: Promise, status, and challenges.* Journal of Nuclear Materials, 2018. **501**: p. 13-30.

4. Grosse, M.M., et al., *Investigation of Corrosion and High Temperature Oxidation of Promising ATF Cladding Materials in the Framework of the Il Trovatore Project.* Top Fuel 2019, Seattle, WA, September 22-27, 2019, 2019: p. 274-279.

5. Tang, C., et al., *Protective coatings on zirconium-based alloys as accident-tolerant fuel (ATF) claddings.* Corrosion Reviews, 2017. **35**(3): p. 141-165.

6. Gao, Z., et al., *Comparison of the oxidation behavior of a zirconium nitride coating in water vapor and air at high temperature.* Corrosion Science, 2018. **138**: p. 242-251.

7. Gao, Z., et al., *Sputter-deposited nitrides for oxidation protection in a steam environment at high temperatures.* Thin Solid Films, 2019. **688**: p. 137439.

8. Jin, D., et al., *A study of the zirconium alloy protection by Cr_3C_2–NiCr coating for nuclear reactor application.* Surface and Coatings Technology, 2016. **287**: p. 55-60.

9. Park, J.-H., et al., *High temperature steam-oxidation behavior of arc ion plated Cr coatings for accident tolerant fuel claddings.* Surface and Coatings Technology, 2015. **280**: p. 256-259.

10. Mayrhofer, P.H., et al., *Microstructural design of hard coatings.* Progress in Materials Science, 2006. **51**(8): p. 1032-1114.

11. Gleiter, H., *Nanostructured materials basic concepts and microstructure.* Acta Materialia, 2000. **48**: p. 1-29.

12. Patscheider, R.H.J., *From Alloying to Nanocomposites—Improved Performance of Hard Coatings.* Advanced Engineering Materials 2000. **2**: p. 247-259.

13. Pomerance, H., *Thermal Neutron Capture Cross Sections.* Physical Review, 1952. **88**(2): p. 412-413.

14. Musil, J., *Hard nanocomposite coatings: Thermal stability, oxidation resistance and toughness.* Surface and Coatings Technology, 2012. **207**: p. 50-65.

15. Musil, J., J. Vlček, and P. Zeman, *Hard amorphous nanocomposite coatings with oxidation resistance above 1000°C.* Advances in Applied Ceramics, 2013. **107**(3): p. 148-154.

16. Pélisson-Schecker, A., H.J. Hug, and J. Patscheider, *Morphology, microstructure evolution and optical properties of Al–Si–N nanocomposite coatings.* Surface and Coatings Technology, 2014. **257**: p. 114-120.

17. Honghua Du, R.E.T., Karl E. Spear, Carlo G. Pantano, *Oxidation studies of crystalline CVD silicon nitride.* Journal of The Eletrochemical Society 1989. **136**: p. 1527-1536.

18. Horton, R.M., *Oxidation kinetics of powdered silicon nitride.* journal of the american ceramic socisty 1968. **52**: p. 121-124.

19. Huang, J.-H., C.-H. Ma, and H. Chen, *Effect of Ti interlayer on the residual stress and texture development of TiN thin films.* Surface and Coatings Technology, 2006. **200**(20-21): p. 5937-5945.

20. Gerth, J. and U. Wiklund, *The influence of metallic interlayers on the adhesion of PVD TiN coatings on high-speed steel.* Wear, 2008. **264**(9-10): p. 885-892.

21. Sivabharathy, M., et al., *Thermal Expansion Studies on Zircaloy-2.* Materials Today: Proceedings, 2016. **3**(9): p. 3064-3070.

22. Sylvia M. Johnson, D.J.R., *Mechanical properties of joined silicon nitride.* Journal of the American Ceramic Socisty, 1985. **68**: p. 468-472.

23. Daniel, R., et al., *Thermal stability of magnetron sputtered Zr–Si–N films.* Surface and Coatings Technology, 2006. **201**(6): p. 3368-3376.

24. Zeman, P. and J. Musil, *Difference in high-temperature oxidation resistance of amorphous Zr–Si–N and W–Si–N films with a high Si content.* Applied Surface Science, 2006. **252**(23): p. 8319-8325.

25. Musil, J., et al., *Properties of magnetron sputtered Al–Si–N thin films with a low and high Si content.* Surface and Coatings Technology, 2008. **202**(15): p. 3485-3493.

26. Gao, Z., et al., *A conformable high temperature nitride coating for Ti alloys.* Acta Materialia, 2020. **189**: p. 274-283.

27. Chen, Z., et al., *A review on the mechanical methods for evaluating coating adhesion.* Acta Mechanica, 2013. **225**(2): p. 431-452.

28. Garner, A., et al., *The microstructure and microtexture of zirconium oxide films studied by transmission electron backscatter diffraction and automated crystal orientation mapping with transmission electron microscopy.* Acta Materialia, 2014. **80**: p. 159-171.

29. Bertoti, I., *Characterization of nitride coatings by XPS.* Surface and Coatings Technology, 2002. **151-152**: p. 194-203.

30. Pezzotti, G., et al., *Human osteoblasts grow transitional Si/N apatite in quickly osteointegrated Si3N4 cervical insert.* Acta Biomater, 2017. **64**: p. 411-420.

31. Lange, A.P., et al., *Structure and chemistry of aluminum predose layers in AlN epitaxy on (111) silicon.* Acta Materialia, 2016. **115**: p. 94-103.

32. Fouad Attar, T.J., *Adhesion evaluation of thin ceramic coatings on tool steel using the*

scratch testing technique. Surface and Coatings Technology, 1996. **78**: p. 87-102.

33. Le Flem, M., J. Canel, and S. Urvoy, *Processing and characterization of Zr3Si2 for nuclear applications.* Journal of Alloys and Compounds, 2008. **465**(1-2): p. 269-273.

34. Zhou, B. and K. Feng, *Zr–Cu alloy filler metal for brazing SiC ceramic.* RSC Advances, 2018. **8**(46): p. 26251-26254.

35. Cheng, B., Y.-J. Kim, and P. Chou, *Improving Accident Tolerance of Nuclear Fuel with Coated Mo-alloy Cladding.* Nuclear Engineering and Technology, 2016. **48**(1): p. 16-25.

36. Zhao, H.L., M.J. Kramer, and M. Akinc, *Thermal expansion behavior of intermetallic compounds in the Mo–Si–B system.* Intermetallics, 2004. **12**(5): p. 493-498.

37. Gianchandani, P.K., et al., *Joining of SiC, alumina, and mullite by the Refractory Metal—Wrap pressure‐less process.* International Journal of Applied Ceramic Technology, 2020. **17**(3): p. 980-989.

38. Castanho, S.M., Moreno, R., Fierro, J.L.G, *Influence of process conditions on the surface oxidation of silicon nitride green compacts.* J. Mater. Sci., 1997. **32**: p. 157-162.

39. Lawniczak-Jablonska, K., Zytkiewicz, Z. R., Gieraltowska, S., Sobanska, M., Kuzmiuk, P., Klosek, K., *Chemical bonding of nitrogen formed by nitridation of crystalline and amorphous aluminum oxide studied by X-ray photoelectron spectroscopy.* RSC Adv., 2020. **10**: p. 27932.

40. Batra, N., Gope, J., Vandana, Panigrahi. J., Singh, R., Singh, P. K., *Influence of deposition temperature of thermal ALD deposited Al2O3 films on silicon surface passivation.* AIP Adv., 2015. **5**: p. 067113.

41. Simonsen, M.E., Sonderby, C., Li, Z., Sogaard, E. G., *XPS and FT-IR investigation of silicate polymers.* J Mater Sci, 2009. **44**: p. 2079–2088.

42. Hultman, L., *Thermal stability of nitride thin films.* Vacuum, 2000. **57**: p. 1-30.

43. Matzke, H., *Diffusion in carbides and nitrides: unsolved problems.* Defect and Diffusion Forum, 1992. **83**: p. 111-130.

44. Wei-E Wang and D.R. Olander, *Computational thermodynamics of the Zr-N systrem* Journals of Alloys and Compounds, 1995. **224**: p. 153-158.

45. Anttila, A., J. Raisanen, and J. Keinonen, *Diffusion of nitrogen in Zr and Hf.* Journal of the Less-Commn Metals, 1984. **96**: p. 257-286.

46. Evans, J.H. and B.L. Eyre, *The heat of solution and diffusivity of nitrogen in molybdenum* Acta Materialia, 1969. **17**: p. 1109-1115.

47. Steinbrueck, M., F.O. da Silva, and M. Grosse, *Oxidation of Zircaloy-4 in steam-nitrogen mixtures at 600–1200 °C.* Journal of Nuclear Materials, 2017. **490**: p. 226-237.

48. Duriez, C., D. Drouan, and G. Pouzadoux, *Reaction in air and in nitrogen of pre-oxidised Zircaloy-4 and M5™ claddings.* Journal of Nuclear Materials, 2013. **441**(1-3): p. 84-95.

49. Grabowski, K.S., A.D.F. Kahn, and E.P. Donovan, *Thermal stability of silicon nitride coatings produced by ion assisted deposition.* Nuclear Instruments and Methods in Physics Research 1989. **B39**: p. 190-193.

50. Kuptsov, K.A., et al., *Structural transformations in TiAlSiCN coatings in the temperature range 900–1600 °C.* Acta Materialia, 2015. **83**: p. 408-418.

51. Luo, L., et al., *Atomic origins of water-vapour-promoted alloy oxidation.* Nat Mater, 2018. **17**(6): p. 514-518.

52. Opila, E.J., *Oxidation and Volatilization of Silica Formers in Water Vapor.* Journal of the American Ceramic Society, 2003. **86**: p. 1238-1248.

53. Mouche, P.A. and K.A. Terrani, *Steam pressure and velocity effects on high temperature silicon carbide oxidation.* Journal of the American Ceramic Society, 2019. **103**(3): p. 2062-2075.

54. Terrani, K.A., et al., *Silicon Carbide Oxidation in Steam up to 2 MPa.* Journal of the American Ceramic Society, 2014. **97**(8): p. 2331-2352.

55. Hay, R.S., *Crystallization kinetics for SiO_2 formed during SiC fiber oxidation in steam.* Journal of the American Ceramic Society, 2019. **102**(9): p. 5587-5602.

56. Cao, F., et al., *Effects of water vapor on the oxidation and the fracture strength of SiC layer in TRISO fuel particles.* Journal of the American Ceramic Society, 2017. **100**(5): p. 2154-2165.